NASA Contractor Report 175051

Grain Boundary Oxidation and an Analysis of the Effects of Pre-oxidation on Subsequent Fatigue Life

(NASA-CR-175051) GRAIN BOUNDARY OXIDATION AND AN ANALYSIS OF THE EFFECTS OF PRE-OXIDATION ON SUBSEQUENT FATIGUE LIFE (Syracuse Univ., N. Y.) 38 p HC A03/MF A01 CSCL 11F G3/26
N86-21654
Unclas
05655

Yoshiki Oshida and H.W. Liu
Syracuse University
Syracuse, New York

February 1986

Prepared for
Lewis Research Center
Under Grant NAG 3-348

National Aeronautics and Space Administration

Grain Boundary Oxidation and an Analysis of the Effects of Pre-oxidation on Subsequent Fatigue Life

Yoshiki Oshida and H.W. Liu[1]

Syracuse University
Syracuse, New York 13210

Abstract

A mechanistic study on the effects of pre-oxidation on subsequent fatigue life was conducted. The surface oxidation and grain boundary oxidation of a nickel-base superalloy (TAZ-8A) were studied at 600 to 1000°C for 10 to 1000 hours in air. The surface oxides were identified and the kinetics of surface oxidation was discussed.

The grain boundary oxide penetration and morphology were studied. The pancake type grain boundary oxide penetrates deeper and its size is larger, therefore, it is more detrimental to fatigue life than the cone-type grain boundary oxide. The oxide penetration depth, a_m, is related to oxidation temperature, T, and exposure time, t, by an empirical relation of the Arrhenius type. The effects of T and t on the statistical variation of a_m were analyzed according to the Weibull distribution function. Once the oxide is cracked, it serves as a fatigue crack nucleus. The statistical variation of the remaining fatigue life, after the formation of an oxide crack of a critical length, is related directly to the statistical variation of grain boundary oxide penetration depth.

[1]Research Assistant Professor and Professor of Mechanical Engineering.

I. INTRODUCTION

Fatigue life is often shortened at elevated temperatures. The shortened fatigue life is usually attributed to oxidation and/or creep. Creep deformation creates grain boundary voids, which is said to weaken the material. In conjunction with the applied cyclic fatigue load, the grain boundary voids may accelerate the initiation and the propagation of fatigue cracks, and thereby shorten fatigue life. The subject of creep-fatigue interaction has been studied extensively (1,2,3,4,5).

In a vacuum of 10^{-8} torr, the effects of cyclic frequency and test temperature on fatigue lives of A286 at elevated temperatures are minimal in comparison with those in air (6,7). Therefore oxidation is more detrimental, at least for some materials, than creep.

This paper deals with surface and grain boundary oxidation and the analysis of the effects of the grain boundary oxidation on fatigue life.

Gibb's free energies of metal oxide formation are negative. No metal or alloy is stable when exposed to an oxidizing environment. Hence a high oxidation resistance of an alloy implies a low oxidation rate. A low oxidation rate is generally due to the slow diffusion rate through the oxide film.

Because grain boundary is a path of rapid diffusion, grain boundary oxidation rate is higher and grain boundary oxide penetration is deeper than the surface oxidation. When an oxide reaches a critical size at an applied stress level, the oxide

will fracture (8). The oxide crack may serve as a nucleus of a fatigue crack, and will grow by the subsequent cyclic fatigue load. Therefore, an oxide crack may shorten fatigue life, and grain boundary oxide penetration depth can serve as a "measure" of high temperature fatigue damage.

McMahon and Coffin (9) have shown ruptured oxide film to act as a fatigue crack nucleus. Shida et al. (10) and Stott et al. (11) have studied grain boundary oxidation. In this paper, a mechanistic study on the effects of pre-oxidation on subsequent fatigue life was conducted. The surface and grain boundary oxidations of a nickel-base superalloy (TAZ-8A) were investigated. The surface oxides were identified by an electron-probe x-ray energy dispersion spectrometry analysis, oxide weight gain and weight loss analysis, and reflection electron diffraction method. The three-dimensional grain boundary oxide morphology was studied. The grain boundary oxidation kinetics was analyzed, and the statistical distribution of the grain boundary oxide penetration depth was studied. The effects of oxide penetration depth and oxide crack on subsequent fatigue life are discussed.

II. SURFACE OXIDATION

A nickel-base superalloy (TAZ-8A) was subjected to high temperature oxidation in air under the stress-free condition. The chemical composition of TAZ-8A is listed in Table 1. The oxidation temperatures were 600, 700, 800, 900, and 1000°C, controlled within ± 8°C. The oxidation time varied from 10 to 1000 hours.

The average weight gain per unit surface area, ΔW_{+0} (mg/cm^2), due to both surface and grain boundary oxidations was obtained for each disk coupon, 15 mm in diameter and 5 mm in thickness. At a given temperature, a linear relationship between the square of ΔW_{+0} and oxidation exposure time, t, was found, Figure 1. The slopes of the lines in the figure are known as the parabolic rate constant, K_p. The data in the figure indicate that the oxidation of TAZ-8A obeys the parabolic rate law as many other superalloys and refractory materials do. The parabolic oxidation rate implies that the oxidation is controlled by diffusion.

Figure 2 shows the parabolic rate constant versus inverse absolute temperature of TAZ-8A and several other superalloys. The data of TAZ-8A seem to follow two line segments similar to Mar-M200. Additional studies are needed to verify whether these two line segments indicate two different oxidation kinetics in the high and low temperature regimes.

The measured weight gain during oxidation, ΔW_{+0}, reflects the amount of oxygen that reacted with the substrate to form an oxide. On the other hand, the weight loss of the substrate due

to the oxidation can be measured by descaling. For rapid descaling, the oxidized sample was immersed into an acid aq. solution (50% HCl, 49% H_2O, 1% H_2O_2) at 70°C (12) for three minutes and subsequently in a solution of 30% HNO_3, 10% H_2O_2, 10% H_3PO_4 and 50% CH_3COOH at 90°C (12) for three additional minutes. The descaling process was followed by an examination with an optical microscope. If the amount of oxide removal was not enough, this process was repeated. The final descaling process is accomplished at a much slower rate by cathodic descaling to avoid the removal of the substrate; oxidized sample at cathode; lead plate at anode; 5% H_2SO_4 electrolyte; and 1 mA/cm^2 current density (13).

The measured weight loss, ΔW_{-M}, reflects the amount of metal loss due to oxidation. The weight gain to weight loss ratio, $\Delta W_{+O}/\Delta W_{-M}$, should be equal to the atomic weight ratio of oxide if the oxide is stoichiometric. The measured ratios are 0.32, 0.44, and 0.49 for oxides formed at 600°, 800°, and 1000°C, respectively. The atomic weight ratio for Cr_2O_3 is 0.462. Similar ratios of other oxides are 0.273 (NiO), 0.889 (Al_2O_3), and 0.393 ($NiCr_2O_4$).

The reflection electron diffraction pattern identified that the outermost layer of the surface oxide formed at 800°C for 960 hours consists mainly of Cr_2O_3 (corundum type of sesquioxide) with a small amount of spinel type oxide possibly such as $NiO \cdot Cr_2O_3$ or $NiO \cdot (Cr,Al)_2O_3$. Some of chromium ions in Cr_2O_3 might be substituted by aluminum ions to form $(Cr,Al)_2O_3$.

Figure 3a shows the picture of a cross-section, under an optical microscope, of a test coupon oxidized at 1000°C for 500 hours. Figure 3b is the cross-section under a scanning electron microscope. The microstructures of the substrate shows the hardening precipitates (γ'-phase or Ni_3Al) in γ-phase matrix with relatively large carbides. After the sample was oxidized, the decomposition of γ'-phase and the chromium depletion were observed in a substrate layer next to the substrate-oxide interface. By increasing the oxidation temperature and prolonging oxidation time, these microstructural changes due to high temperature oxidation became remarkable.(e.g., the thickness of 100 μm of γ'-phase decomposition zone was observed after 1000°C × 960 hours oxidation.)

Figure 4 shows the line profiles for NiK_α, CrK_α and AlK_α constructed from the electron-probe spot analyses by an x-ray energy dispersion spectrometer. The spot analyses were made at five locations on each one of the three test coupons oxidized at 600, 800 and 1000°C. The five locations are: (1) in the substrate far away from the substrate-oxide interface, (2) and (3) next to the substrate-oxide interface, one in the substrate and the other in the oxide, (4) at the mid-section of the surface oxide layer, and (5) at the outermost layer of the surface oxide. The oxide layer at 600°C is thin; the spots (4) and (5) merged together.

The major findings from the spectrometric analysis are as follows:

i) The oxides of aluminum, nickel and chromium are present in the surface oxide layer. However, at 600°C, nickel oxide is the dominant component, at 800°C and 1000°C chromium oxide is the dominant one.

ii) At 800 and 1000°C, the chromium concentration increases continuously from the substrate to the outermost layer of the surface oxide with a minor chromium depleted zone in the substrate next to the substrate-oxide interface.

iii) At 800 and 1000°C, the concentrations of the chromium oxide at the outermost layers of the surface oxides are much higher than that of either the aluminum or nickel oxides.

iv) The concentration of nickel decreases continuously from the substrate to the outermost layer of the surface oxide.

This spectrometric analysis indicates that the oxides formed at 800°C and 1000°C in air are mainly Cr_2O_3 or $(Cr,Al)_2O_3$ with a much less amount of $NiO \cdot Cr_2O_3$ and/or $NiO \cdot (Cr,Al)_2O_3$. This is consistent with the measured weight gain/weight loss ratio, if the relative amounts of the various oxides are taken into consideration. For example, at 1000°C, the relative portions of the chromium, nickel, and aluminum oxides are 2:1:1. This will give a weight gain to weight loss ratio of 0.52, which is very close to the measured ratio of 0.49. The activation energy in Figure 2 in the high temperature regime is very close to the activation energies of the diffusion of chromium in either Cr_2O_3 or $NiO \cdot Cr_2O_3$ (14).

At 600°C, the spectrometric analysis indicates that nickel oxide is the dominant component, and the ratio ($\Delta W_{+O}/\Delta W_{-M}$) is 0.32, which is between the values of NiO (0.273) and $NiO \cdot Cr_2O_3$ (0.393). Therefore, in the low temperature regime, it is speculated that the oxidation kinetic is controlled by the diffusion of nickel atoms through the oxide layer.

III. GRAIN BOUNDARY OXIDATION

Figure 5 shows a picture of an oxidized surface. The grain boundary oxide penetrated much deeper than the surface oxide. A cracked grain boundary oxide can serve as a nucleus, which will grow by the subsequent fatigue cycles, and will shorten the fatigue life. Fatigue crack growth rate is related to ΔK, and ΔK is related to the size and shape of the micro-crack. Therefore the shape and the depth of oxide penetration at grain boundaries are important factors for fatigue life prediction.

The three-dimensional shapes and sizes of the grain boundary oxides were traced optically. First a microhardness indentation was placed close to the oxide to be studied, and the size and shape of the oxide on the surface were traced. After the initial measurements, the surface was mechanically polished. The thickness of the surface layer polished off can be monitored by the change in the size of the hardness indentation. After polishing, the size and shape of the oxide were traced again. This process was repeated to trace the three-dimensional morphology of the grain boundary oxides. As shown in Figures 6 and 7, two types of grain boundary oxides have been observed; the cone type and the pancake type. The pancake type was larger, seemed to penetrate deeper, and due to its shape and size, would have a higher value of stress intensity factor and would reduce fatigue life more than the cone type.

The aspect ratio a/b varies widely. On the average, a/b is close to one (15). However, the ratios for the deeper oxides are much larger than one, often in the range of 10 to 20 or more (see Figure 5). The depth of penetration by grain boundary diffusion depends on the misorientation of the two neighboring grains (16, 17). Conceivably, the depth of grain boundary oxide is also dependent on the misorientation.

Oxide depth is also a function of oxidation temperature and the length of the time of exposure. At a given temperature and exposure time, the oxide depth varied widely from one grain boundary to another. The deepest grain boundary oxide crack will control the amount of the reduction in fatigue life. Therefore, the extreme value, i.e., the deepest oxide penetration should be analyzed. In this paper, the grain boundary oxide depth as a function of oxidation temperature and exposure time, grain boundary oxidation kinetics and the statistical distribution and the extreme value of grain boundary oxide depth were studied.

The statistical distribution of grain boundary oxide penetration was studied at exposure times from 100 to 1000 hours and at temperatures of 600, 800 and 1000°C. Cylindrical test coupons were oxidized in air. The oxidized disk coupons were sectioned, each sectioned surface was examined under an optical microscope, and the maximum grain boundary oxide penetration depth, a_{mi}, of the sectioned surface "i" was measured. Then a thin layer of the coupon approximately 80 μm thick was ground

off, the new surface was polished, and another a_{mi} of the new surface was measured. This process was repeated many times (often 12 times) for each test coupon to collect enough data for the statistical analysis. The grain size of the nickel alloy is between 50 to 80 μm. After a removal of 80 μm, an entirely new set of grain boundaries was exposed. Therefore each sectioned surface can be considered as an independent sample.

Let N be the total number of sectioned surfaces examined. The measured a_{mi}'s are ranked from the shallowest penetration depth to the deepest penetration. M_i is the ranking number for a_{mi}.

For a large number of sectioned surfaces, the probability of finding an oxide depth less than a_{mi} is $P(a_{mi}) = P(a)_i \approx M_i/(1+N)$. The probability of having a depth equal to or deeper than a_{mi} is $[1 - P(a)_i]$.

Weibull assumes the distribution function

$$[1 - P(a)_i] = \exp\left[-\frac{(a_{mi} - a_u)^b}{a_o}\right] \qquad (1)$$

and

$$\ln \ln \frac{1}{[1 - P(a)_i]} = b \ln (a_{mi} - a_u) - \ln a_o \qquad (2)$$

In a Weibull plot of $\ln \ln [1/\{1 - P(a)_i\}]$ versus $\ln (a_{mi} - a_u)$, Equation (2) gives a straight line. a_u is the horizontal shift for each of the data points, so that all the points will be on a straight line in the plot. The term a_o

sets the scale of the plot. The term b is the slope of the line and is called shape parameter or Weibull modulus, a_u and a_o are location parameter and scale parameter, respectively.

Figure 8 shows the Weibull plot for 480 data points at 800°C for 500 hours. Before the shift, the data points follow a curve A in the right hand side of the figure. After the shift of a_u (40 μm) the straight line B correlates well with the data points. The vertical spread of the data points, especially at the lower end of the line, is caused by a large number of measurements having the same depth. The difference in depths between neighboring points could not be resolved easily with the microscope used. The three parameters were observed as follows: b = 2.0, a_u = 40 μm and a_o = 740 μm.

The statistical distribution of a_{mi} at each of the test conditions can be analyzed according to the Weibull plot (Figure 8). Twelve plots are needed to analyze the combinations of three oxidation temperatures and four exposure times. The amount of analysis could become overwhelmingly large if wide ranges of temperatures and exposure times are needed, and the applications of such results could be complicated. Therefore, it is desirable to develop a simplified data correlation method.

The oxide depth a_{mi} has been measured from 100 to 1000 hours at 600, 800 and 1000°C. It is assumed that the relation between a_{mi}, t and T has the form

$$a_{mi} = \alpha_i \, t^n \exp\left(-\frac{Q}{RT}\right) \qquad (3)$$

The regression analysis of the data gives the following empirical relation.

$$a_{mi}(cm) = 1.34 \times 10^{-3} t^{0.25} \exp(-4.26/RT) \qquad (4)$$

t in seconds, the activation energy in kcal/mol, and T in ^{o}K. The coefficient of correlation is 0.96. The plot of $\ln (a_{mi}/t^{0.25})$ versus (1/T) is shown in Figure 9. The slope of the line is (4.26/R).

Grain boundary diffusion can be considered as a channeled one-dimensional flow, with a constant concentration, C_o at the interface between the surface oxide layer and the substrate (see Figure 10). The oxygen concentration in the grain boundary is (18)

$$C(x,t) = C_o \left[1 - \text{erf}\left(\frac{x}{2\sqrt{D_{gb}t}}\right)\right] \qquad (5)$$

where erf is the error function and D_{gb} is the grain boundary diffusion coefficient. The oxygen in the grain boundary will form bulk oxide if the concentration reaches a certain critical value C_c. According to Equation (5),

$$C_c = C_o \left[1 - \text{erf}\left(\frac{x_c}{2\sqrt{D_{gb}t}}\right)\right] \qquad (6)$$

x_c is the depth of the oxide penetration, where $C = C_c$.

The quantity $x_c/2\sqrt{D_{gb}t}$ is a constant and x_c must be proportional to $\sqrt{D_{gb}t}$. This is different from Eq. (4)

The orientation of the grain boundary oxide is determined by the orientation of the substrate grain into which the oxide is growing. The orientations of the two halves of the grain boundary oxide growing into two "neighboring" substrate grains are different, and an oxide grain boundary exists between these two halves. The diffusion of oxygen will pass through the oxide grain boundary. The oxygen in the grain boundary oxide will diffuse into the substrate by bulk diffusion.

Equations (4) and (5) are true only for a one-dimensional diffusion flow. The grain boundary oxidation is further complicated by the bulk diffusion of oxygen outward from the grain boundary oxide into the substrate.

Figure 10 shows an element of the grain boundary, $\Delta x \times \Delta y$. The diffusion coefficient D_{gb}, is much larger than the bulk diffusion coefficient D_b, often several orders of magnitude larger. The large aspect ratio, a/b, in Figure 5, indicates that the flux along the grain boundary is much larger than the flux into the substrate. Whipple (19) has taken the bulk diffusion into consideration in his analysis of grain boundary diffusion. According to his study, the oxide penetration depth is affected by the bulk diffusion. However, the extent of the effect has to be assessed quantitatively for TAZ-8A. In addition, the chemical process of oxidation and its effect on the gradient of chemical potential have yet to be studied. For the moment, Equation (4) can be treated as an empirical relation.

The empirical relation (4) correlates the data reasonably well. However, sizable scatter is shown in Figure 9. It is well known that grain boundary diffusion is a function of the relative orientations of the two neighboring grains. Couling and Smoluchowski (16) measured grain boundary diffusion penetration of radioactive silver in copper as a function of the angle of (100) tilt boundaries. Their results are shown in Figure 11. Turnbul and Hoffman (17) have shown that the activation energy of grain boundary diffusion is a function of the angle of misorientation, θ. Therefore, the activation energy Q in Equation (3) is not a constant but dependent on θ. Since we are measuring the deepest oxide penetration, perhaps Q is close to the minimum value. However, a statistical variation of Q from one cross-section to another is expected.

The dependence of a_{mi} on t is closely related to the oxide morphology. For example the dependence on t for the cone type oxide will be different from the pancake type. The detailed oxidation process, the oxide structures and the effect of bulk diffusion will affect the dependence of a_{mi} on both t and T.

Equation (4) is an empirical equation that correlates the measured oxide penetration. The deviation from the empirical relation of each measurement can be lumped into the term α_i

$$\alpha_i = a_{mi} t^{-n} \exp\left(\frac{Q}{RT}\right) \qquad (7)$$

At any temperature T and exposure time t, with each of the measured a_{mi}, the value of α_i can be calculated with the empirically determined constants n and Q. The Weibull plot of all of the 144 values of α_i of 12 data sets of 12 data points each is shown in Figure 12. The values of b, α_u, α_o are 1.85, 0.53×10^{-3} and 4.8×10^{-6} respectively. It is interesting to note that the b-value of 1.85 for α_i for the 144 data points is close to the average b-value of 1.8 of the 12 data sets for a_{mi}. a_{mi} is linearly proportional to α_i, and the statistical distribution of α_i is directly related to the statistical distribution of a_{mi}.

One may consider the maximum value of α along the periphery of a sectioned surface "i" as the α_i of an area of πDd of the test coupon. D is the coupon diameter and d is the grain size. Another sectioned surface at a distance one grain size away can be considered a section containing an entirely different set of grain boundaries and it is an independent sample.

Let $P(\alpha)$ be the probability of finding the maximum α-value less than α_i on a unit surface area of a test coupon. $P(\alpha)$ is related to the probability of a sectioned surface $P(\alpha)_i$

$$[1 - P(\alpha)_i] = [1 - P(\alpha)]^{\pi Dd} \tag{8a}$$

P_S is the probability of finding an α-value less than α_i on a surface area S.

$$[1 - P(\alpha)_S] = [1 - P(\alpha)]^{S} \tag{8b}$$

and

$$[1 - P(\alpha)_S] = [1 - P(\alpha)_i]^{S/\pi Dd}$$

$$\ln[1 - P(\alpha)_S] = (S/\pi Dd)\ \ln[1 - P(\alpha)_i] \tag{9}$$

We define R,

$$R = -(S/\pi Dd)\ \ln[1 - P(\alpha)_i] \tag{10}$$

Following Equation (1), we have

$$[1 - P(\alpha)_i] = \exp[-(\alpha_i - \alpha_u)^b/\alpha_o] \tag{11}$$

$$R = (S/\pi Dd)[(\alpha_i - \alpha_u)^b/\alpha_o]$$

$$P(\alpha)_S = 1 - \exp(-R) \tag{12}$$

The value of $P(\alpha)_S$ thus obtained can be taken as the value of $P(a)_S$ for the oxide depth $a = \alpha t^n \exp(-Q/RT)$. The $P(a)_S$ thus determined is not the same as the probability of finding an oxide depth less than "a" among a set of measurements determined at a given oxidation temperature and exposure time. It incorporates the additional "uncertainty" of T and t.

Zheng and Liu have studied the fatigue lives of precracked cylindrical specimens. Both the smooth and precracked cylindrical specimens are shown in Figure 13. The specimens were precracked by a jeweler's saw (20).

The measured fatigue reversals, $2N_F$, are shown in Figure 14 as a function of deformation work density, which is $(\Delta\sigma^2/8E + \sigma_{YC}\Delta\varepsilon_p)$. $\Delta\sigma$ is the applied fatigue stress range; E, the Young's modulus; σ_{YC}, the cyclic yield strength; $\Delta\varepsilon_p$, the applied cyclic plastic strain range. The fatigue lives were measured in the low cycle fatigue regime. The straight lines for the smooth and the precracked specimens are parallel in the log-log plot. Thus the ratio between the fatigue lives of the precracked specimens, N_{Fi}, and the fatigue lives of the smooth specimens, N_{Fo} is a constant for a given precrack size, and in general, it is a function of the quantity (a_o/a_i)

$$\frac{N_{Fi}}{N_{Fo}} = F\left(\frac{a_o}{a_i}\right)$$

a_i is the precrack size, and a_o is a fictitious crack size for the "smooth" specimens. The function F can be determined empirically. Once the function is determined, the fatigue life of the preoxidized specimens can be predicted.

If one considers the grain boundary oxide as a precrack of size a_i, a_i is a random variable and is also a function of the time, t, and temperature, T, of oxidation. The remaining fatigue life N_{Fi} of a pre-oxidized specimen must also be a function of t and T, and N_{Fi} must also be a random variable.

A mechanistic model to predict the fatigue life of a pre-oxidized specimen is outlined above. With additional information on the effects of cyclic stress and cyclic strain on oxide crack formation and a mechanistic model of fatigue crack growth at high temperatures, the fatigue life at elevated temperatures can be predicted quantitatively. A mechanistic model of grain boundary oxidation accelerated fatigue crack growth has been proposed by Liu and Oshida (21).

SUMMARY AND CONCLUSIONS

The effects of pre-oxidation on subsequent fatigue life was studied mechanistically. Nickel-base superalloy (TAZ-8A) was subjected to high temperature oxidation (at 600 to 1000°C for 10 to 1000 hours) in air. Surface oxidation kinetics and chemical and structural studies on surface oxides were carried out. In the high temperature regime (i.e., 800 to 1000°C), outward diffusion of chrominum ions through the surface oxide layer appears to control the oxidation kinetics. In the low temperature regime (i.e., 600 to 800°C), nickel ion diffusion through the oxide layer seems to govern the parabolic oxidation rate.

Through the three-dimensional morphological observations, it is found that there exists two different types of grain boundary oxides; cone type and pancake type. The pancake type oxide will be more damaging because of its size and shape.

The grain boundary oxide penetration depth, a_m, is related to oxidation temperature, T, and exposure time ,t, i.e., $a_m = \alpha t^n \exp(-Q/RT)$, with n = 0.25 and Q = 4.26 kcal/mol.

A sufficiently large grain boundary oxide will be cracked by an applied stress. The largest and deepest of the oxide cracks is the most damaging to fatigue life. The statistical analysis using the Weibull distribution function for the grain boundary oxide penetration depth gives the probability of finding an oxide crack of a certain size on a surface area exposed to an oxidation temperature, T, for an exposure time, t. The size of the oxide crack can be related to the remaining fatigue life.

REFERENCES

(1) "Manual on Low Cycle Fatigue Testing" ASTM STP No.465 (1969)

(2) "Symposium on Fatigue at Elevated Temperature" ASTM STP No.520 (1972)

(3) Proc. International Conf. on Creep and Fatigue in Elevated Temperature Applications (1973)

(4) ASME-MPC-3 Symposium on Creep-Fatigue Interaction (1976)

(5) R.M.Pelloux and N.S.Stoloff ed.;"Creep-Fatigue-Environment Interactions" AIME (1980)

(6) L.F.Coffin, Jr.; Proc. of International Conf. on Fatigue: Chemistry, Mechanics and Microstructure, pp.590/680 (1972)

(7) L.F.Coffin, Jr.; Met. Trans., 3, pp.1778/1788 (1972)

(8) S.D.Antolovich, P.Domas and J.L.Strudel; Met. Trans., 10A, pp.1859/1868 (1979)

(9) C.J.McMahon and L.F.Coffin, Jr.; Met. Trans., 1, pp.3443/3450 (1970)

(10) Y.Shida, G.C.Wood, F.H.Stott, D.P.Whittle and B.D.Bastow; Corr. Sci., 21(8), pp.581/597 (1981)

(11) F.H.Stott, G.C.Wood, Y.Shida, D.P.Whittle and B.D.Bastow; Corr. Sci.; 21(8), pp.599/624 (1981)

(12) R.Hales and A.C.Hill; Corr. Sci.; 12, pp.843/853 (1985)

(13) G.R.Rundell; Metal Progress, 127(4), pp.39/54 (1985)

(14) P Kofstad; "Nonstoichiometry, Diffusion, and Electrical Conductivity in Binary Metal Oxides" Wiley-Interscience, NY pp.101/362 (1972)

(15) Y.Oshida and H.W.Liu: "Oxidation and Low Cycle Fatigue Life Prediction", NASA Conf. Pub. 2339 on Turbine Engine Hot Section Technology, pp.321/329 (Oct. 1984)

(16) L.Couling and R.Smoluchowski; J.Appl.Phys., 25, p.1538 (1954)

(17) D.Turnbull and R.Hoffman; Acta Met., 2, p.419 (1954)

(18) P.G.Shewmon; "Diffusion in Solids" McGraw-Hill Book Com., NY (1963)

(19) R.T.P.Whipple; Phil.Mag., 45, p.1225 (1954)

(20) M.Zheng and H.W.Liu; Technical Report NASA Grant No. NAG3-348, "Crack Tip Field and Fatigue Crack Growth in General Yielding and Low Cycle Fatigue", (1984)

(21) H.W.Liu and Y.Oshida; "Grain Boundary Oxidation and Fatigue Crack Growth at Elevated Temperatures" to be published (1985)

Table I Chemical composition (wt. %)

	Ni	Cr	Mo	W	Ta	Cb	Al	C	B
TAZ-8A	68	6	4	4	8	2·5	6	0·12	·004

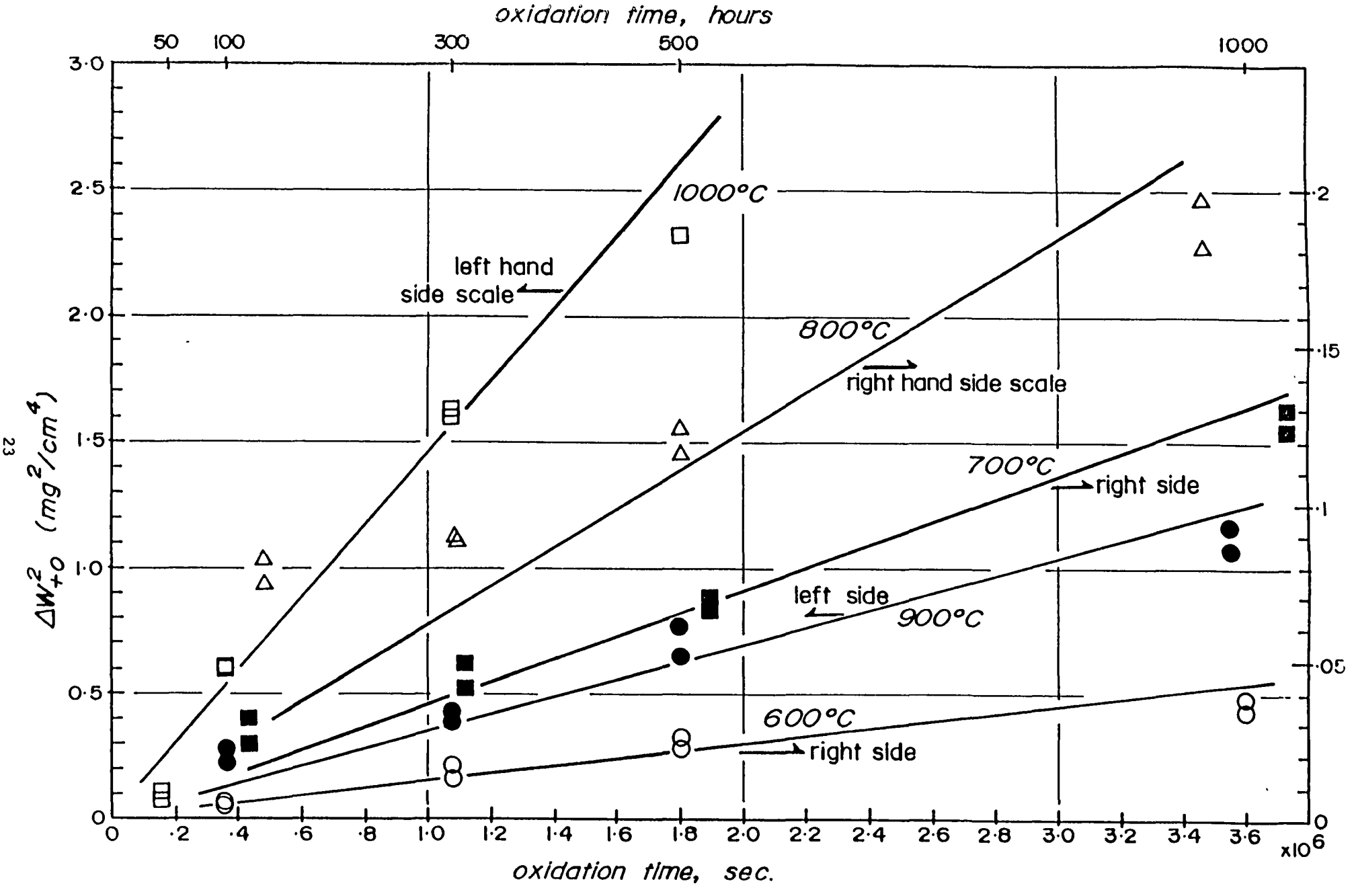

Figure 1 Relationship between the square of weight gain and oxidation exposure time.

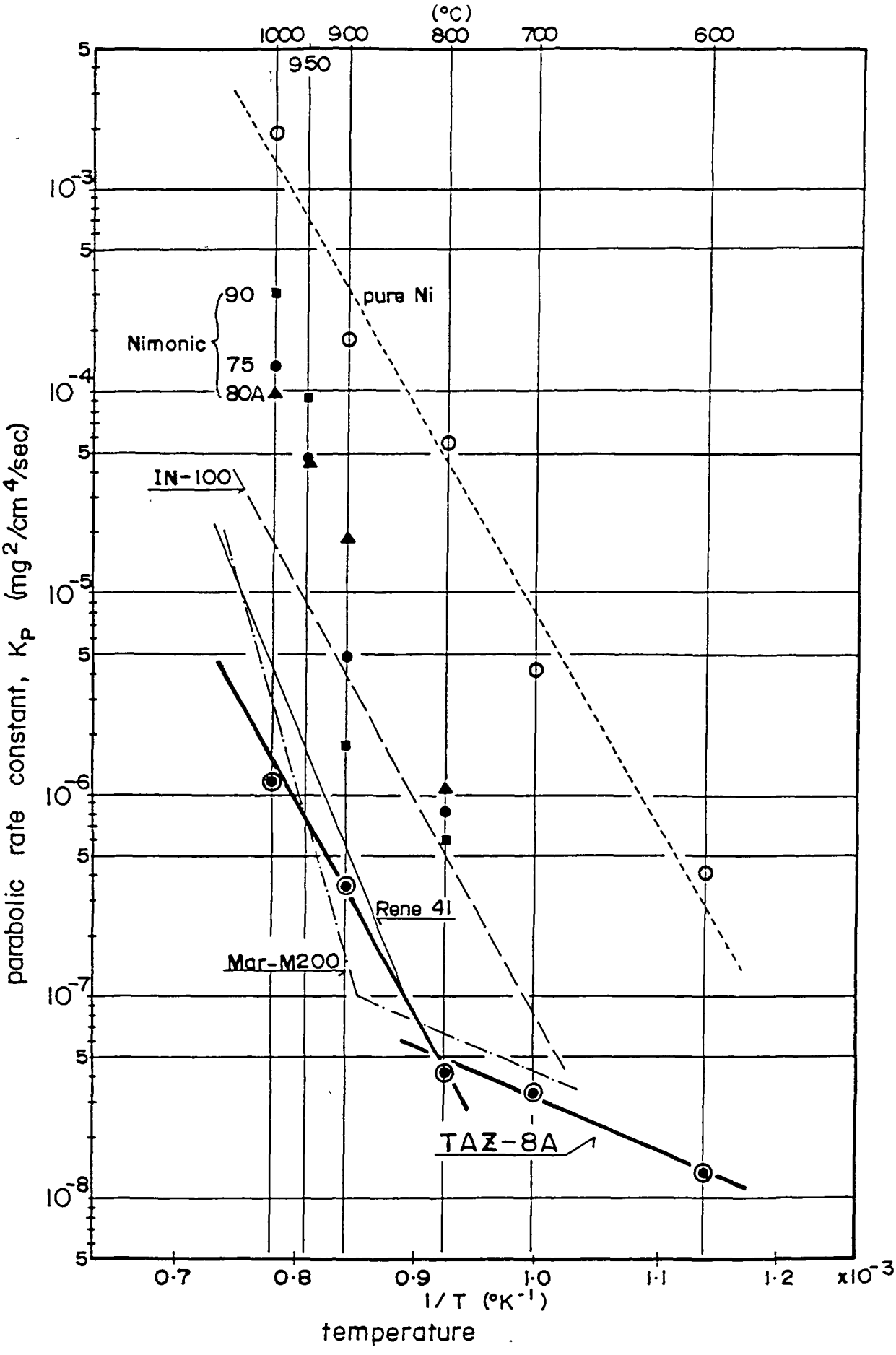

Figure 2 Parabolic rate constant versus inverse absolute temperature

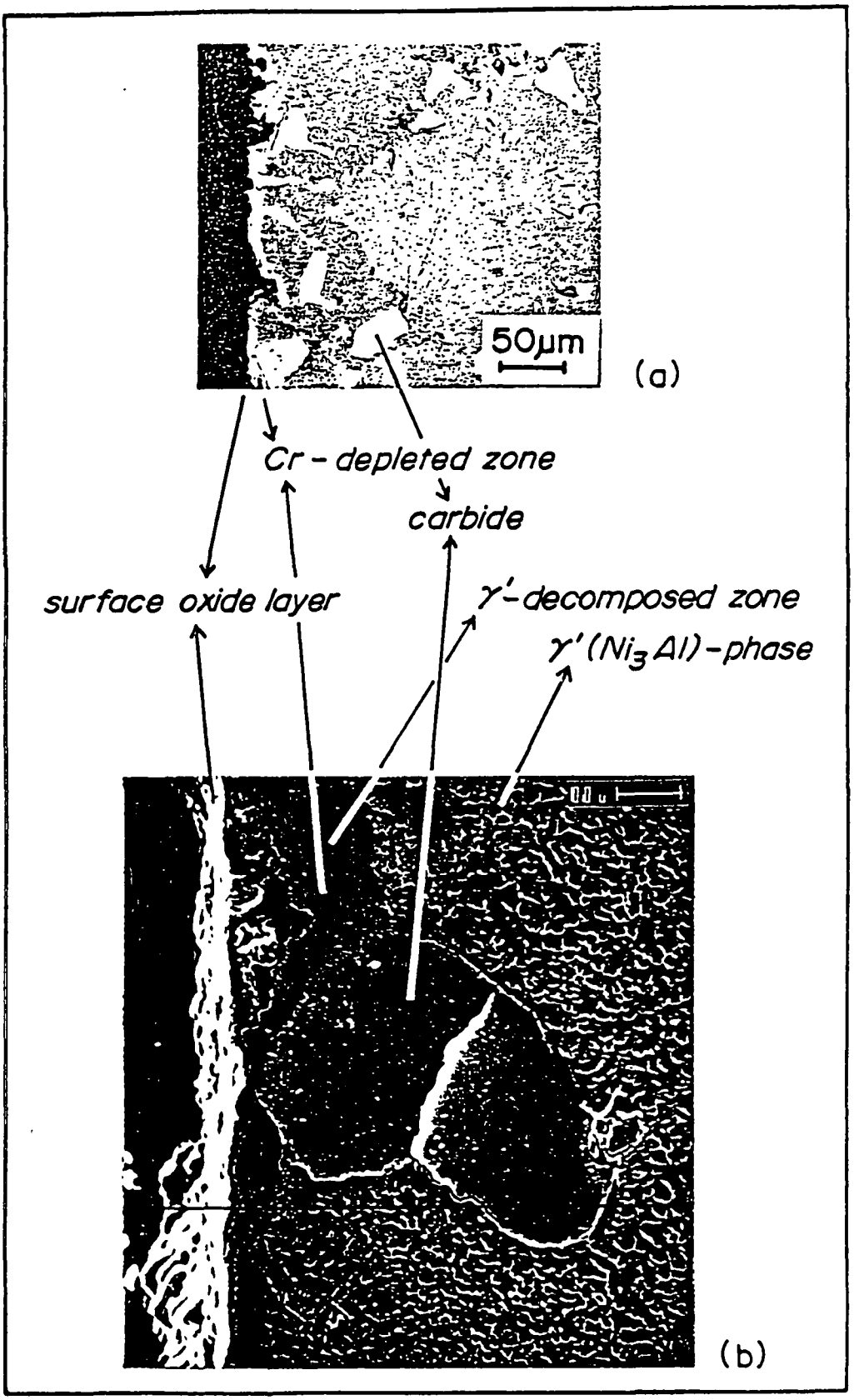

Figure 3 Micrographs of cross-section of a test coupon oxidized at 1000°C for 500 hrs

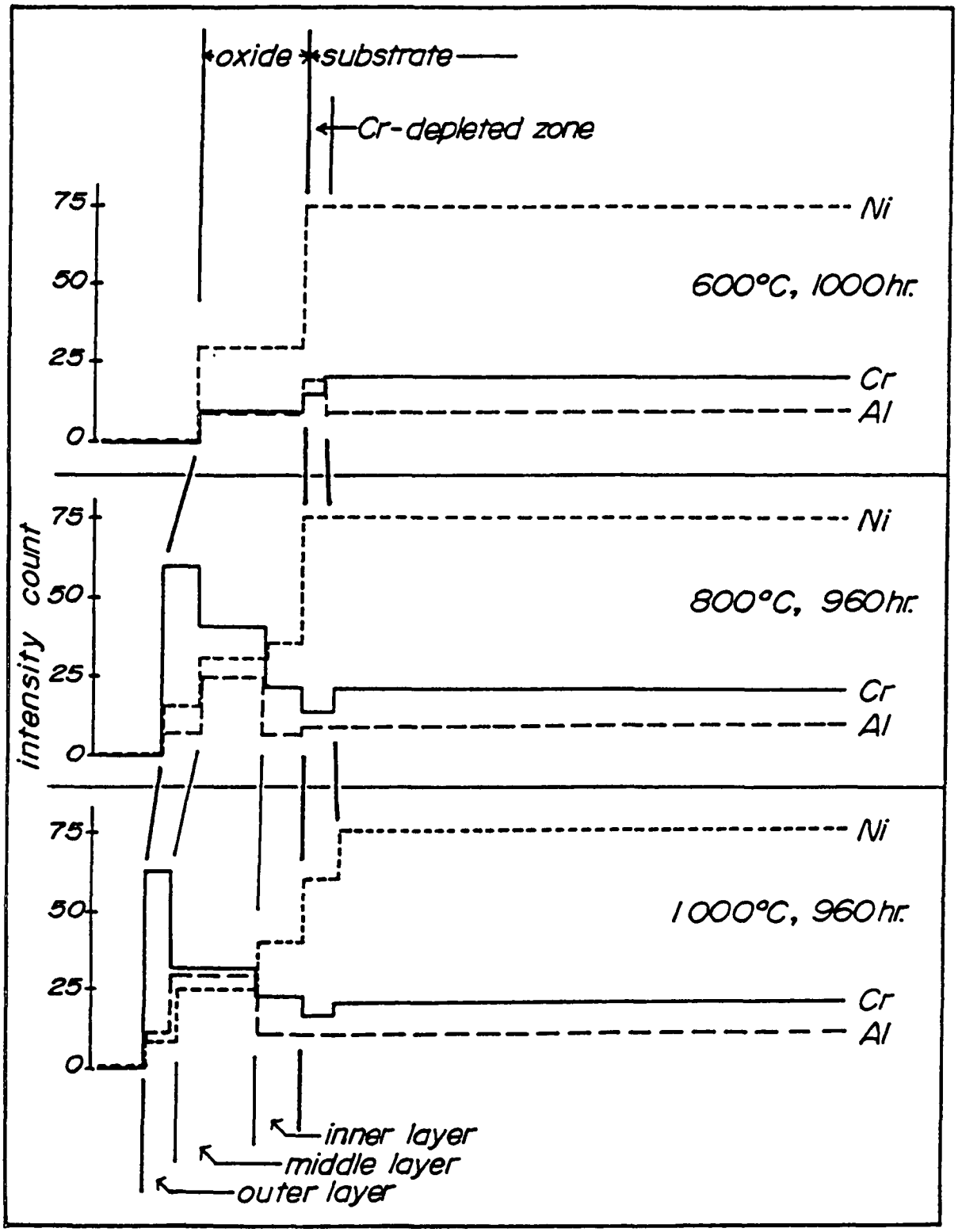

Figure 4 Line profiles of Ni, Cr, and Al on coupons oxidized at three different oxidation conditions

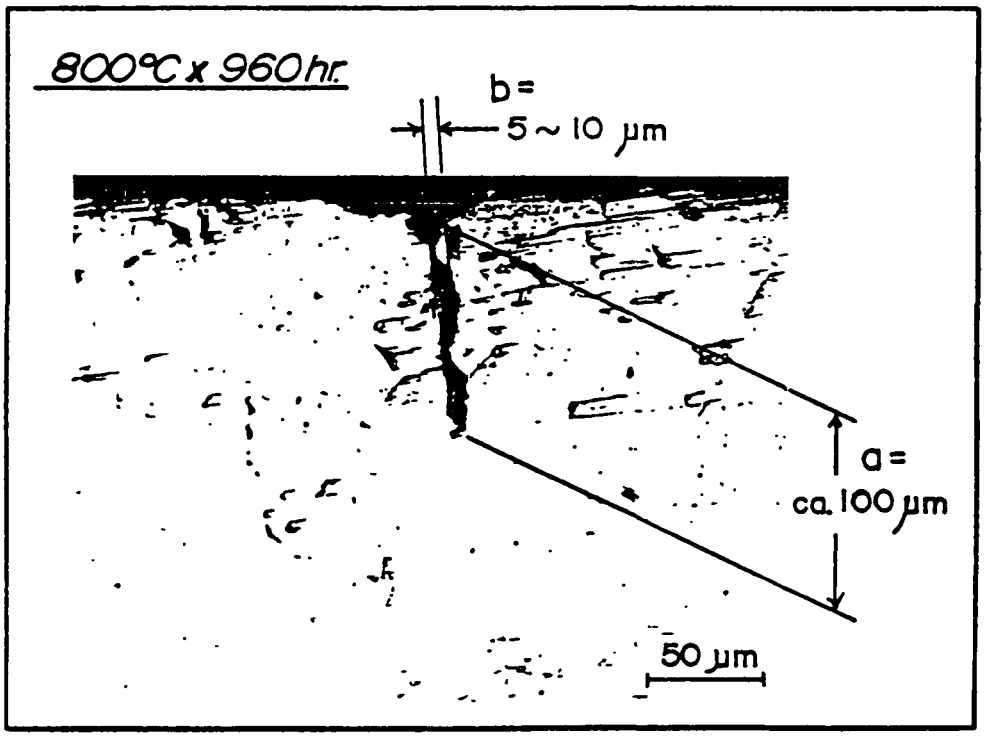

Figure 5 Cross-sectional micrograph, showing a deep penetration by a grain boundary oxidation

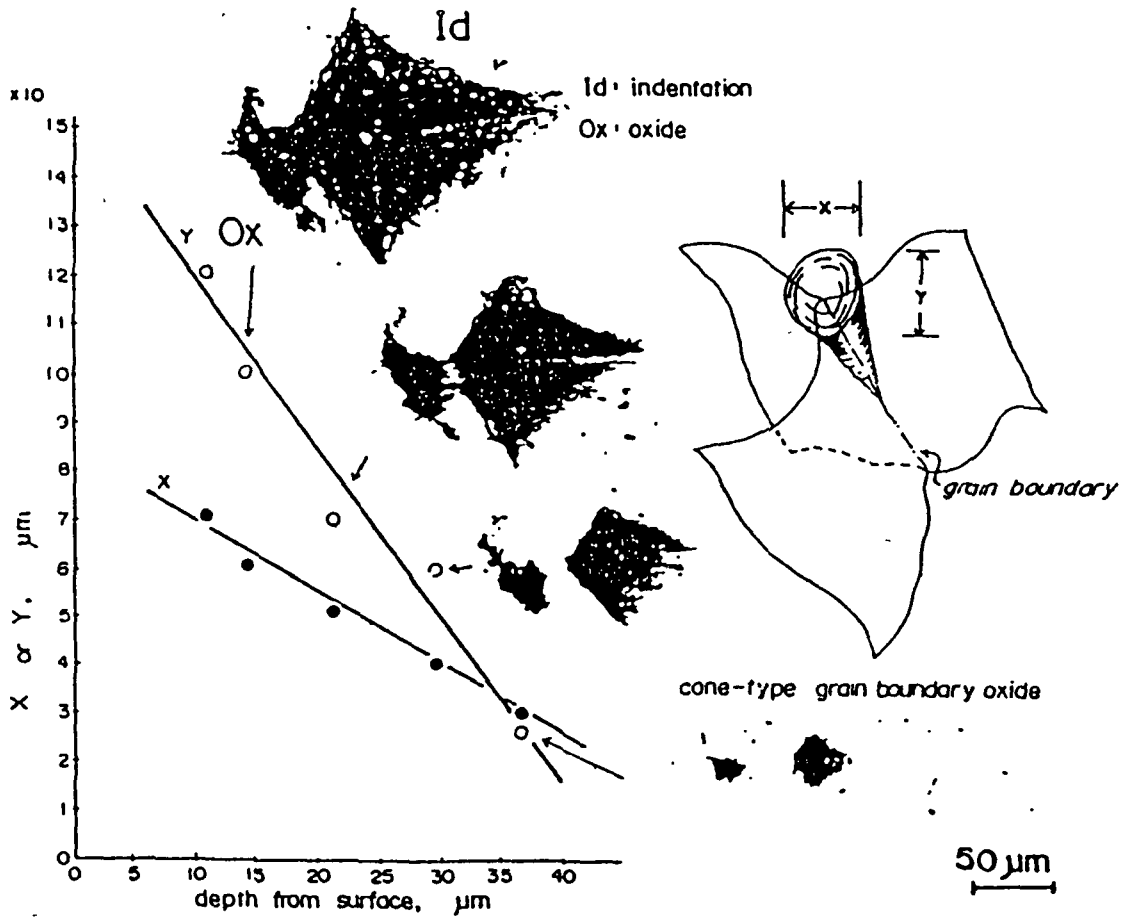

Figure 6 Results of morphological studies on grain boundary oxide, *cone type* grain boundary oxide

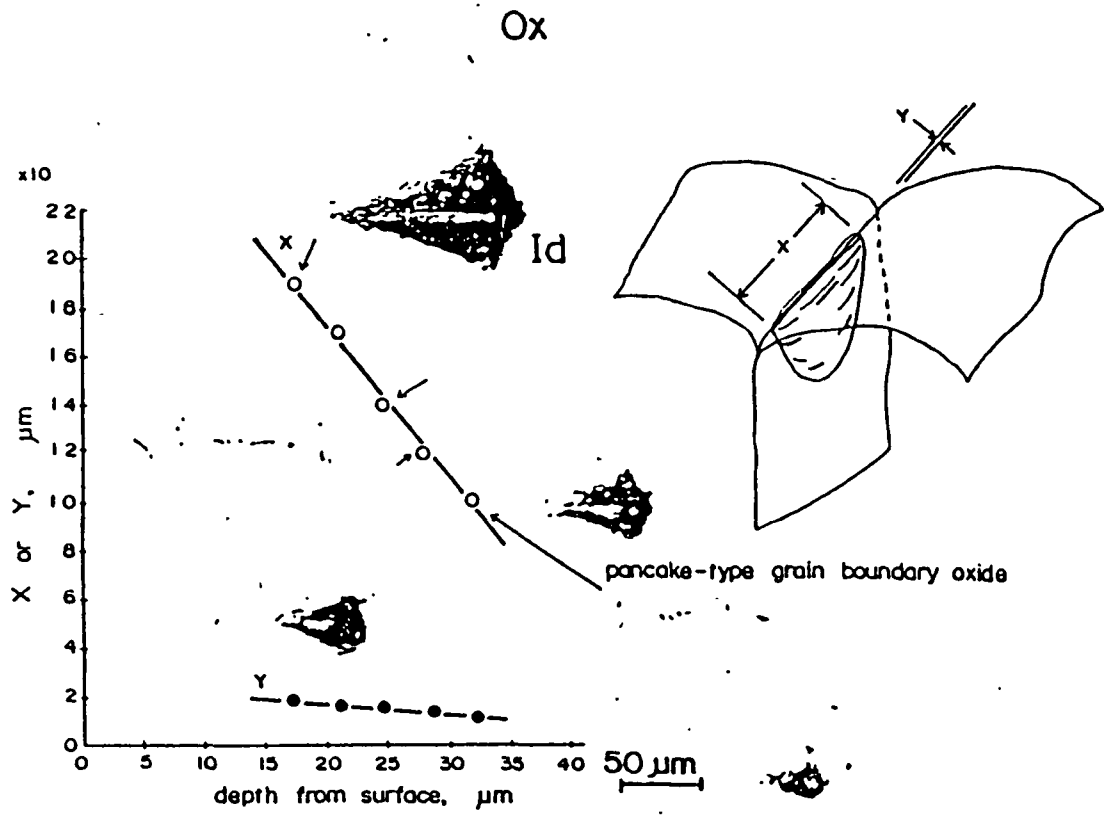

Figure 7 Results of morphological studies on grain boundary oxide, pancake type grain boundary oxide

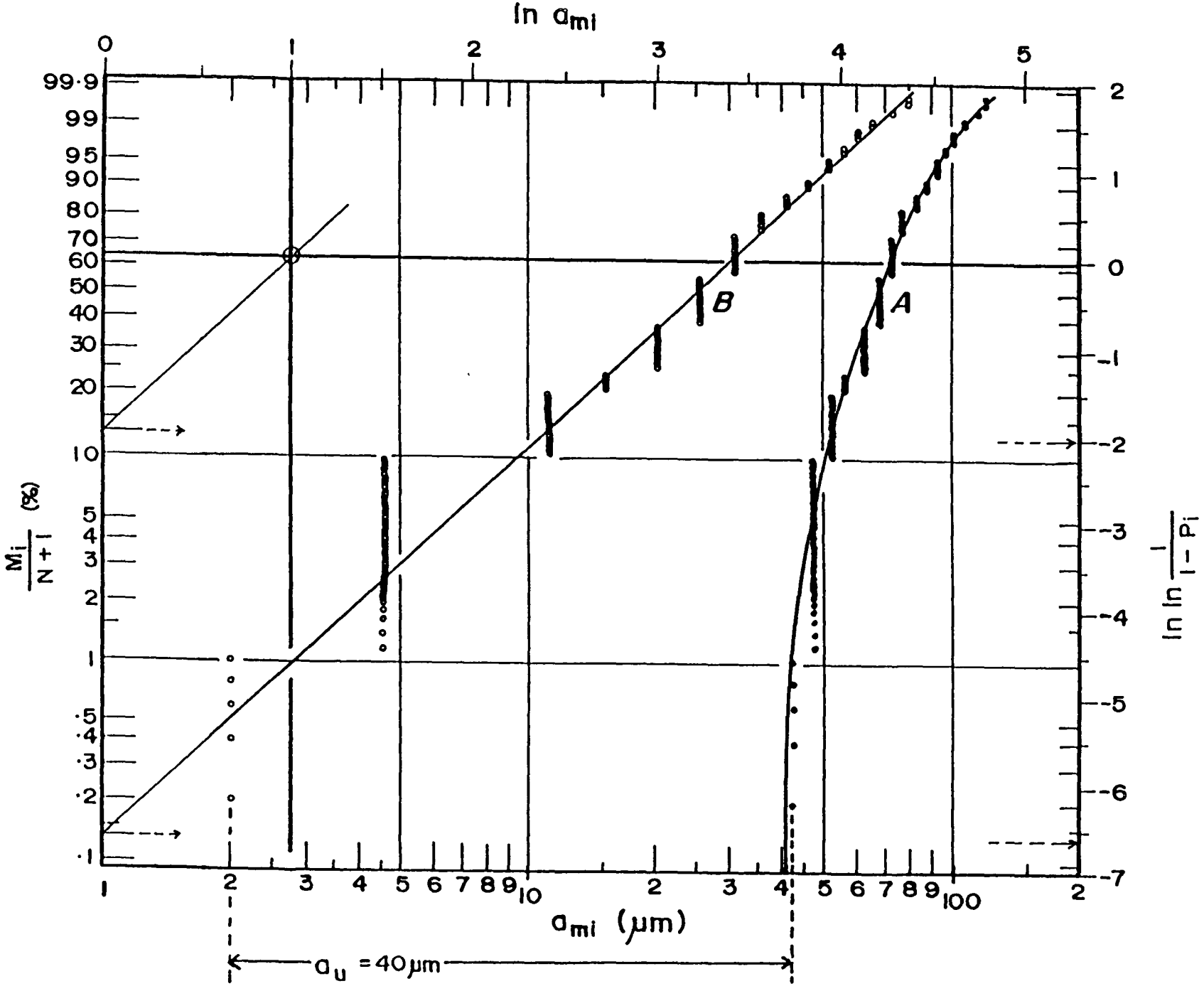

Figure 8 Weibull plot for 480 data points obtained from oxidized coupon at 800°C for 500 hrs

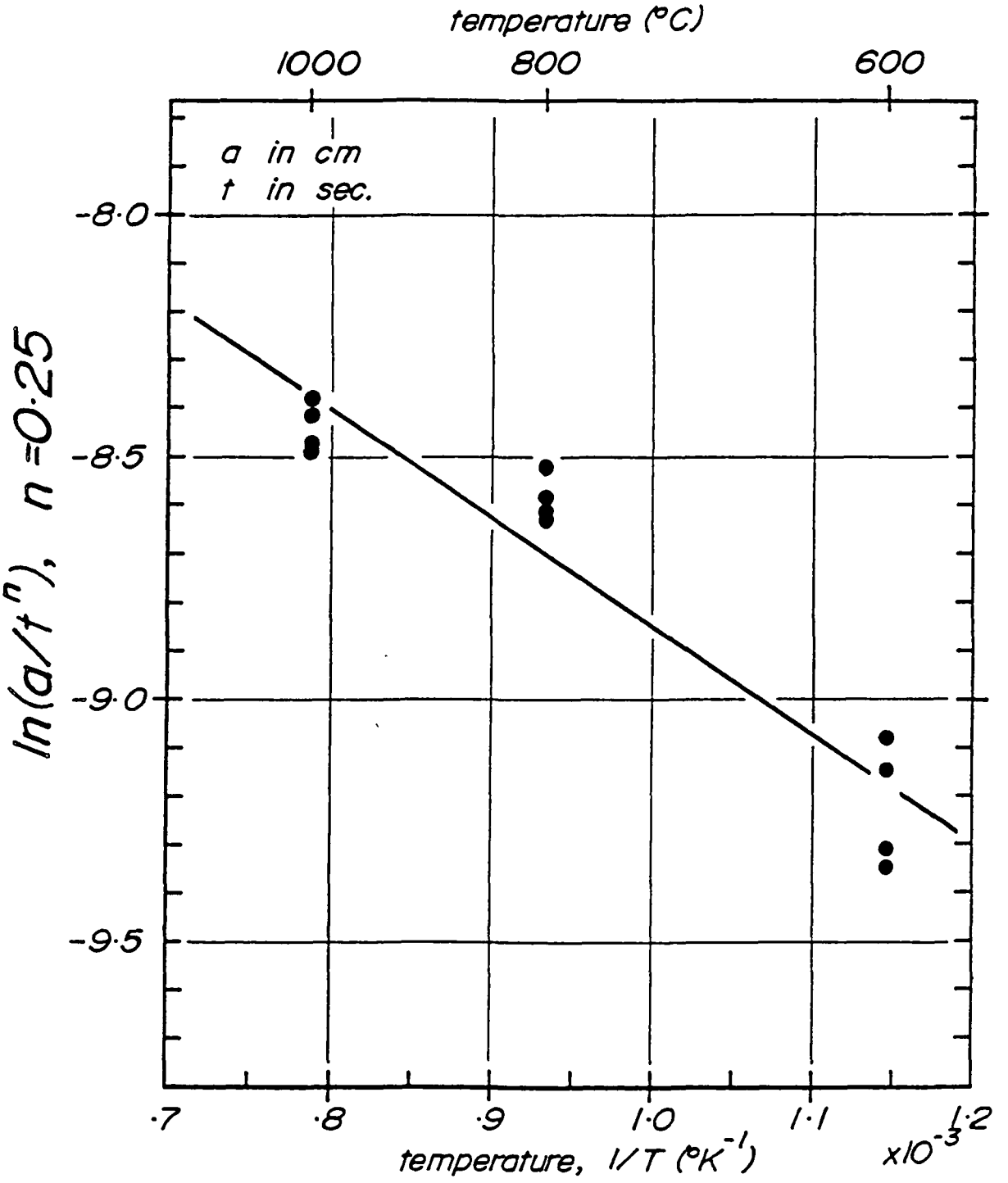

Figure 9 Relationship between $\ln(a_{mi}/t^{0.25})$ versus (1/T)

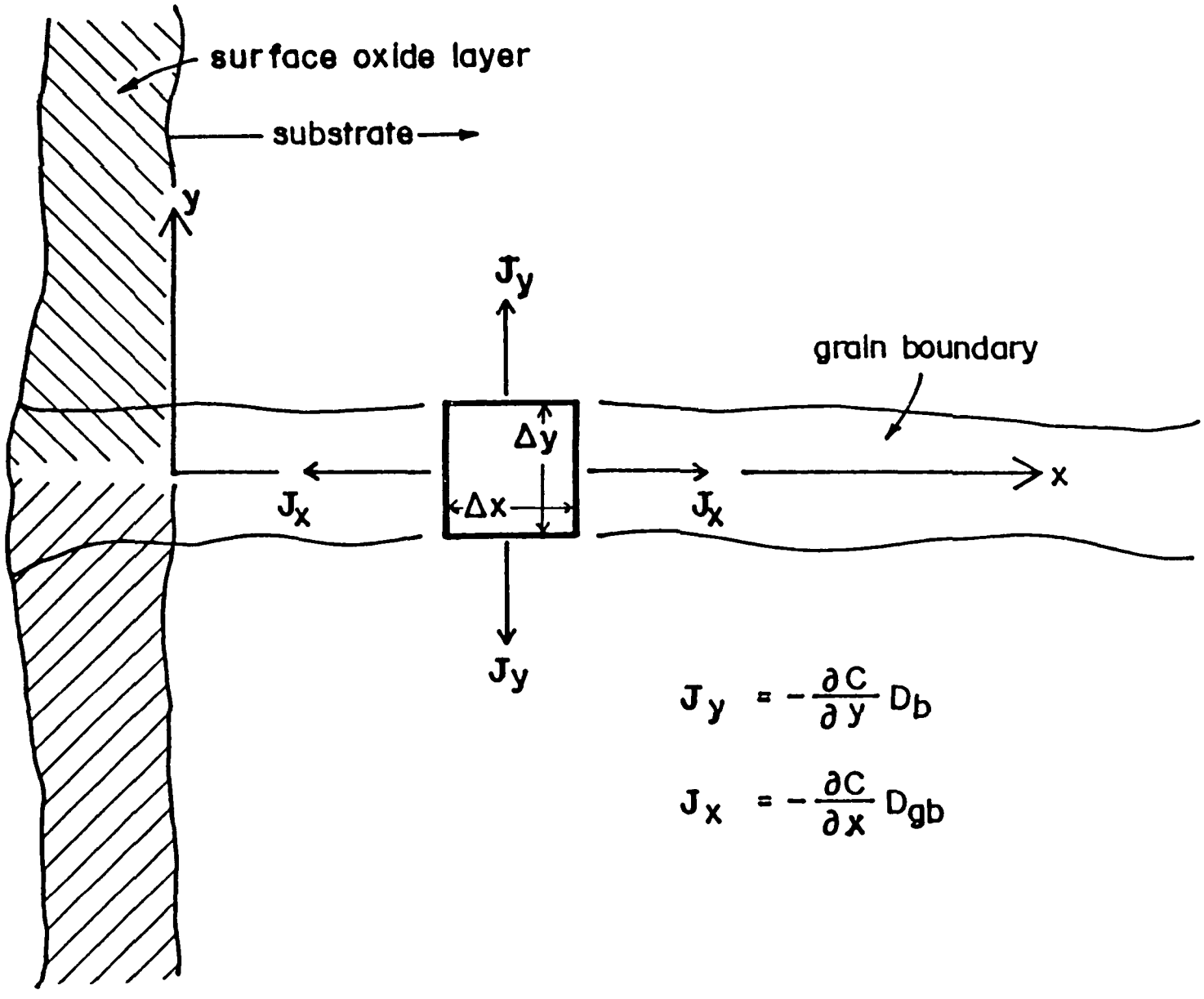

Figure 10 A channeled one-dimensional flow model for grain boundary diffusion

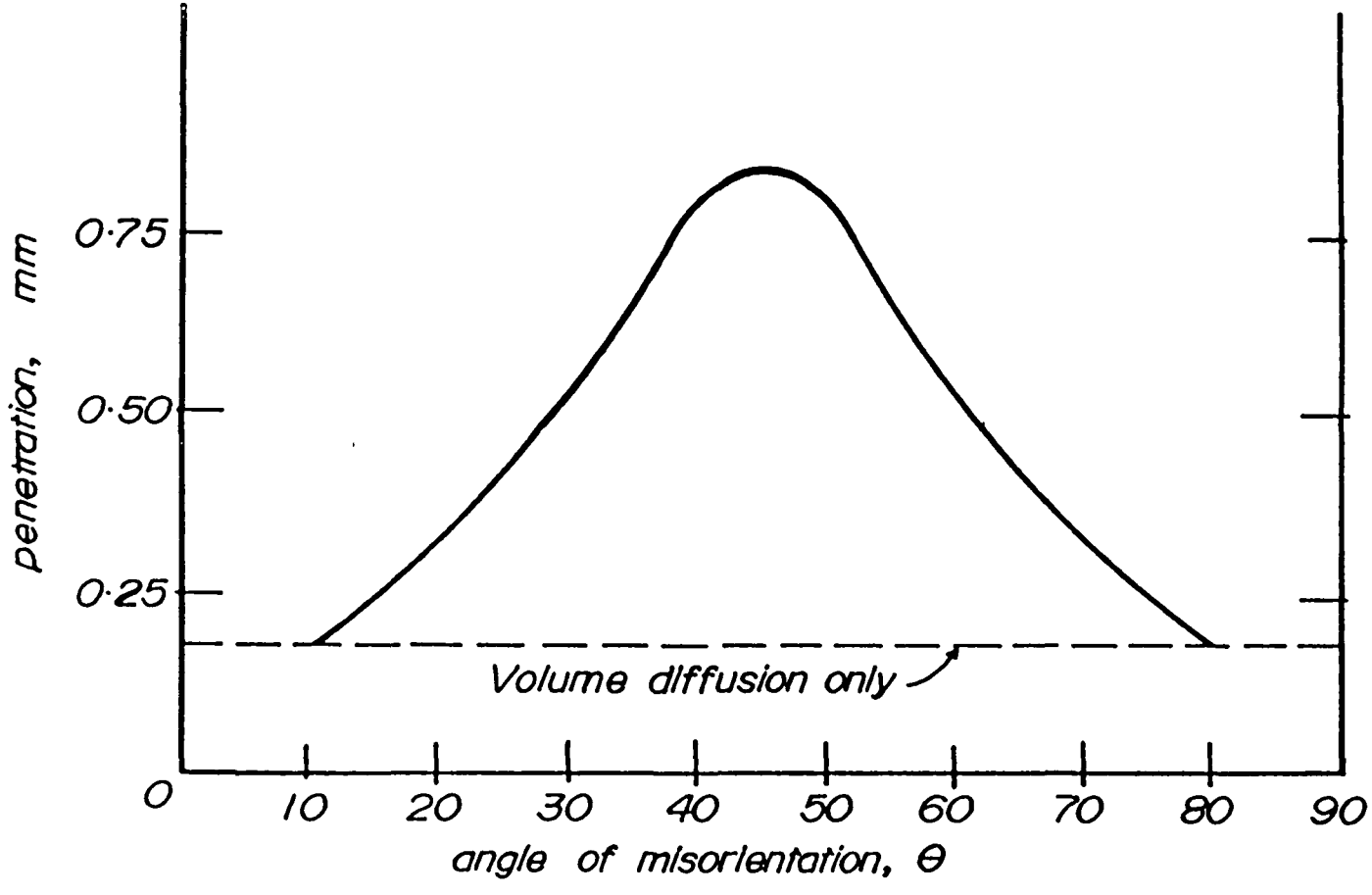

Figure 11 Penetration of silver along (100) tilt boundaries in copper (ref. 16)

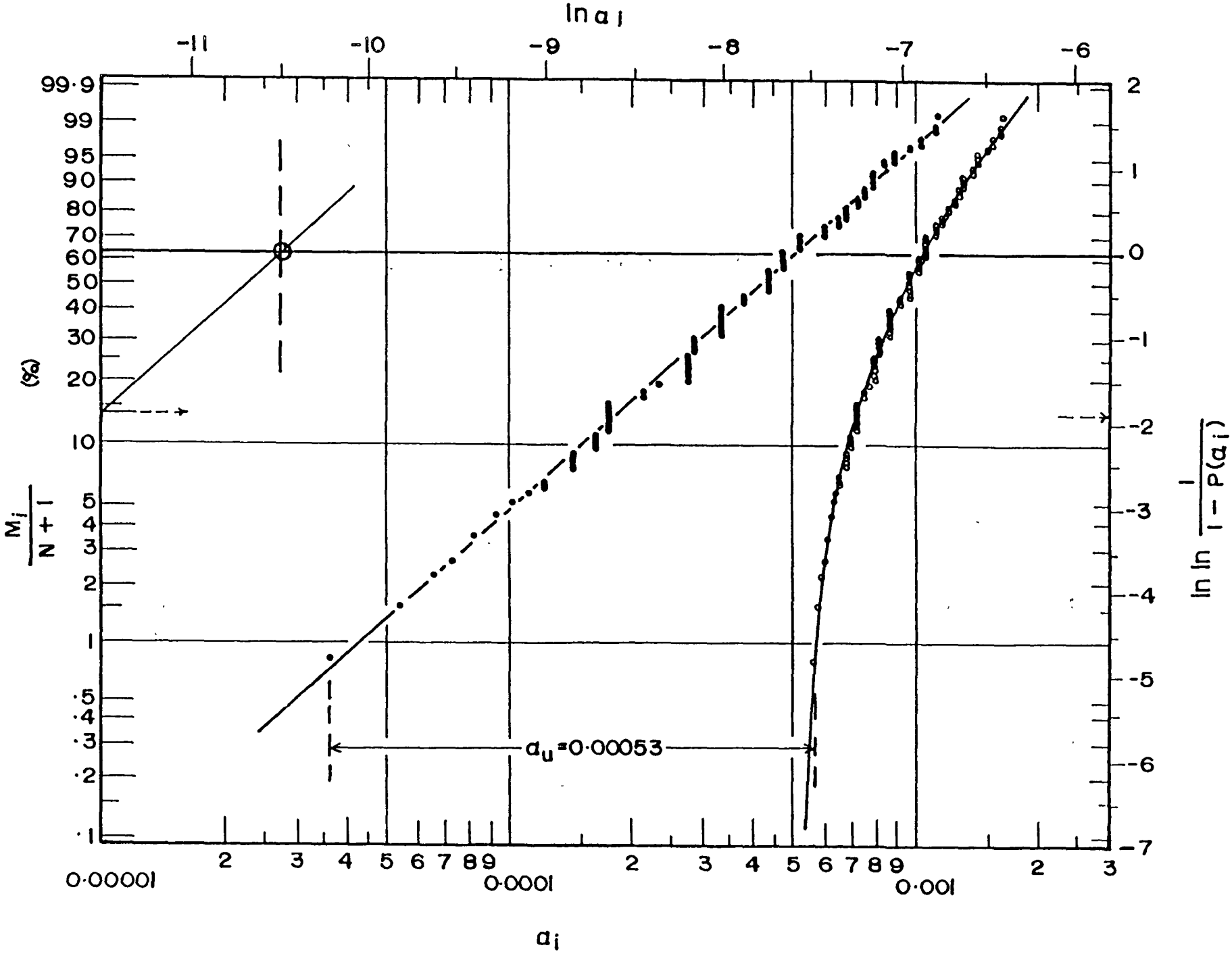

Figure 12 Weibull plot of α_i according to Equation (7)

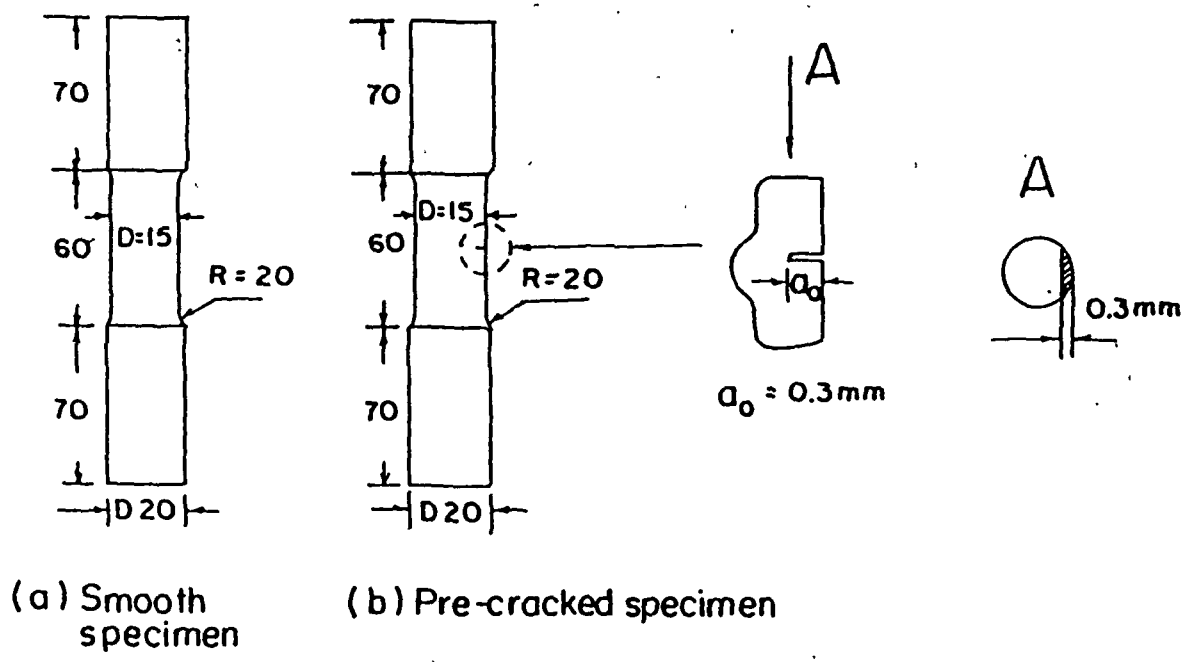

Figure 13 Smooth and precracked low cycle fatigue specimen configurations

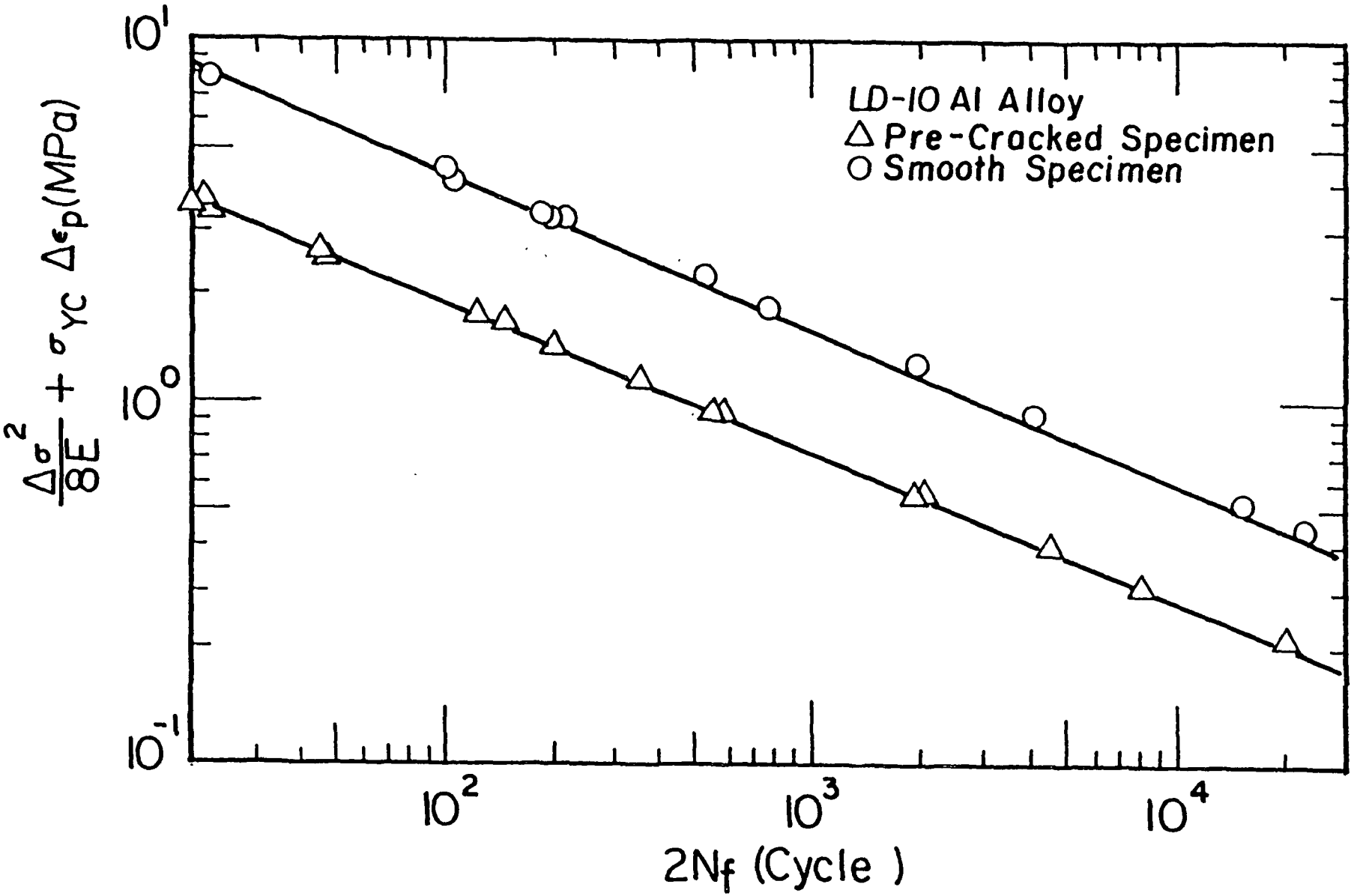

Figure 14 Correlation of $(\Delta\sigma^2/8E + \sigma_{YC}\Delta\varepsilon_p)$ versus $(2N_F)$ for LD-10 aluminum alloy (ref.20)

National Aeronautics and
Space Administration

Lewis Research Center
Cleveland, Ohio 44135

Official Business
Penalty for Private Use $300

SECOND CLASS MAIL

ADDRESS CORRECTION REQUESTED.

Postage and Fees Paid
National Aeronautics and
Space Administration
NASA-451

NASA